photonics

MDPI

Article

Opto-Electronic Duality Principle and Application in SAR Imaging

Huanqin Zhang [1], Yiran Jin [1], Guomin Gao [2,*], Pengfei Wang [2], Jiunan Dong [2], Jiajia Chen [3] and Kaizhi Wang [1,2]

[1] School of Integrated Circuits, Shanghai Jiao Tong University, Shanghai 200240, China
[2] Yiwu Zhiyuan Research Center of Electronic Technology, Yiwu 322000, China
[3] Shanghai Xiaoyuan Innovation Center, Shanghai 200240, China
* Correspondence: kaokuomin@alu.hdu.edu.cn; Tel.: +86-18257667431

Abstract

This paper proposes a novel design principle for spatial optical information processing systems, termed the Opto-Electronic Duality Principle (OEDP). Based on the OEDP, an optical system that is dual-equivalent to a microwave system—referred to as the Opto-Electronic Duality System (OEDS)—can be constructed using optical components. The OEDS employs laser light as the information carrier in place of microwaves, maintaining strict consistency with the microwave system in both signal amplitude and phase. Owing to the inherent reversibility of optical systems, the received microwave signal can be modulated onto a laser beam and, when propagated backward through the OEDS, the microwave response of the detected target is reconstructed and recorded by a camera. Building upon the OEDS, this paper further designs and implements an OEDS specifically for SAR imaging processing, and presents parameter configurations for both airborne and spaceborne scenarios.

Keywords: signal processing; microwave photonics; synthetic aperture radar; Opto-Electronic Duality Principle; spatial light modulator; phase compensation

1. Introduction

Currently, signal processing techniques—including synthetic aperture radar (SAR) imaging—are almost exclusively implemented using digital semiconductor devices, with digital algorithms at their core [1,2]. Figure 1 illustrates the block diagram of a conventional microwave detection system.

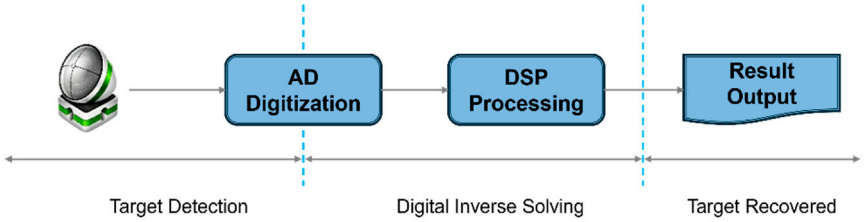


Figure 1. Schematic diagram of a conventional microwave detection system.

As shown in Figure 1, conventional microwave signal processing follows a typical workflow: the received signal is digitized by an AD module and subsequently processed by a DSP module. The essence of this approach is to construct a mathematical (digital) system that is the inverse of the detection process—once the digitized information

Check for updates

Received: 23 September 2026
Revised: 6 November 2026
Accepted: 10 November 2026
Published: 16 November 2026

Copyright: © 2026 by the authors. Licensee MDPI, Basel, Switzerland. This article is an open access article distributed under the terms and conditions of the Creative Commons Attribution (CC BY) license.

is fed into this mathematical system, the target information can be recovered. Therefore, the core of developing such inverse algorithms lies in solving the inverse problem of the detection system. In practice, however, the mathematical expression of this inverse process is often extremely complex, and the resulting inverse algorithms commonly suffer from high computational complexity, pronounced sensitivity to system errors and noise, and limited adaptability—making them difficult to satisfy the demands of high-timeliness and high-reliability applications.

To address these challenges, this paper introduces an optical system—the Opto-Electronic Duality System (OEDS)—constructed using optical components to achieve dual-equivalence with a microwave detection system. Unlike conventional approaches that rely on digital computation, the OEDS performs signal processing in the optical domain, offering the potential for ultra-fast, low-power, and electromagnetic-interference-immune operations. The novelty of this work lies in the systematic extension of this duality framework to the field of SAR echo processing. Specifically, we provide a complete mathematical derivation from the SAR echo signal model to the spatial light modulator (SLM) pixel mapping and the dual-reconstruction condition, and we implement a dedicated OEDS-SAR system with airborne and spaceborne parameter configurations.

The remainder of this paper is organized as follows. Section 2 is devoted to the elaboration of the Opto-Electronic Duality Principle. Section 3 presents the scheme design of the opto-electronic duality system applied to SAR imaging, including the SAR echo signal model, SLM pixel mapping, and the dual-reconstruction condition. Section 4 describes the system implementation and provides parameter analysis for both airborne and spaceborne cases. Finally, Section 5 concludes the paper.

2. Overview

2.1. Opto-Electronic Duality Principle

The Opto-Electronic Duality Principle (OEDP) refers to the dual mapping of the target's spatial position and electromagnetic response in a microwave detection system into the optical domain by optical means, such that the optical space and the microwave space maintain strict consistency in both signal amplitude and phase, thereby forming a physically equivalent optical counterpart to the microwave system [3,4]. Its core idea encompasses three aspects:

- Spatial dual mapping: The spatial coordinates of the target and the propagation path of electromagnetic waves in the microwave domain are mapped to the corresponding spatial positions and optical propagation paths in the optical domain;
- Strict consistency in amplitude and phase: The signals in the optical system maintain precise equivalence with those in the microwave system in both amplitude and phase, ensuring that information is not distorted during domain conversion;
- Physical equivalence: The optical system is not only mathematically equivalent to the microwave system, but also constitutes an equivalent dual system in terms of physical processes.

2.2. Opto-Electronic Duality System

Based on the OEDP, this paper employs optical components to construct a spatial optical processing system that is dual-equivalent to a microwave detection system—the Opto-Electronic Duality System (OEDS).

The OEDS replaces microwaves with laser light as the information propagation medium, maintaining strict consistency with the microwave system in both signal amplitude and phase, thereby forming a physically equivalent optical counterpart. As shown in Figure 2, the microwave system detects the original scene and generates the radar signal,

which is then converted into a spatial optical signal via modulation. The optical signal is subsequently processed by the optical system, and the scene is finally reconstructed in the optical domain. Since optical systems are generally reversible, when the received microwave echo signal is modulated onto a laser beam and propagated backward through the OEDS, the microwave response of the target is reconstructed in the optical domain and recorded by a camera [5].

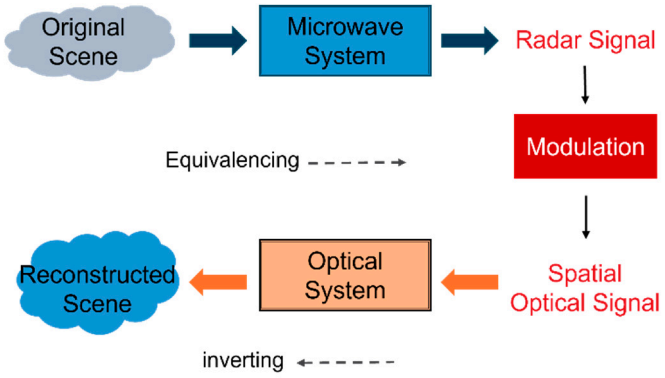


Figure 2. Schematic diagram of the OEDS working principle.

Furthermore, owing to the reversibility of optical paths, the OEDS can simultaneously perform system simulation and signal processing in the optical domain—simply by injecting optical signals in different propagation directions. As shown in Figure 3, forward injection (from the scaled-down scene) yields a simulated radar echo signal, corresponding to system simulation; backward injection (from the radar echo signal) yields the reconstructed scene, corresponding to signal processing.

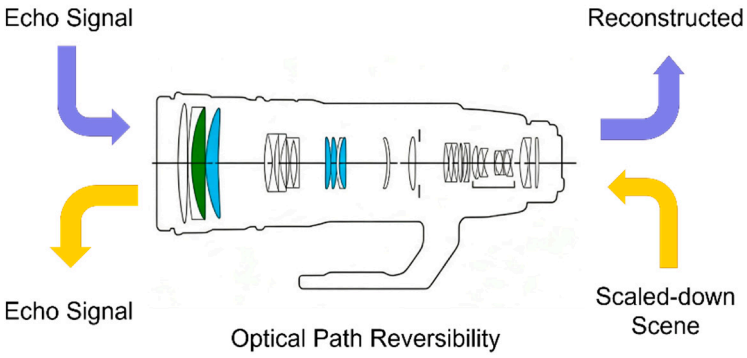


Figure 3. Schematic diagram illustrating the application of optical path reversibility (Yellow arrows: forward injection; Blue arrows: backward injection).

The construction of the OEDS can be understood as using light waves and optical components to build a "scaled-down" version of the radar detection process and its inverse. As illustrated in Figure 4, this scaling effect originates from the wavelength disparity: visible light and microwaves typically differ by five orders of magnitude (a factor of 10^5). Consequently, the microwave detection process, which would otherwise require a large spatial footprint, can be reconstructed with high fidelity within a relatively compact space using an optical system [6,7].

Compared with traditional digital signal processing schemes, the OEDS offers the following significant advantages:

- Simultaneous forward–inverse construction—The inverse process (optical reconstruction) is obtained naturally during the construction of the forward process (microwave

detection), substantially reducing the difficulty of mathematical modeling and algorithm design;

- Ultra-fast processing speed—Since the system is built with optical components, signal processing occurs at the speed of light in the optical domain, making the computational time overhead negligible;
- Extremely low power consumption—Most optical processing elements are passive, so the overall system power consumption remains remarkably low;
- Immunity to interference and radiation—With only a minimal number of digital semiconductor devices, the system has natural resilience against electromagnetic interference and radiation environments.

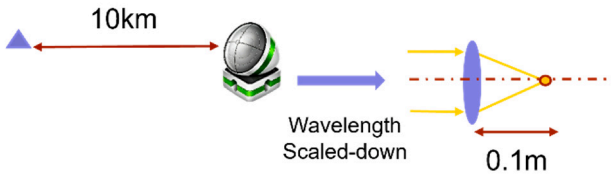


Figure 4. Schematic diagram of the scene miniaturization principle.

3. Method

3.1. OEDS-SAR System

Building upon the OEDS architecture, we extend its application to SAR imaging processing, resulting in the OEDS-SAR system. The OEDS-SAR system differs fundamentally from conventional optical SAR processing systems.

Conventional optical SAR processors—such as the tilted-plane systems and optical 4f architectures developed in foundational works [3,4,8–10]—were primarily designed to physically implement the mathematical algorithms (e.g., frequency-domain matched filtering or cross-correlation) of digital SAR signal processing. They essentially function as complex analog optical computers, mimicking the mathematical operations required to focus SAR phase histories.

In contrast, the OEDS-SAR does not mimic signal processing algorithms. Instead, it is constructed as a physically equivalent inverse system of the microwave detection process. The OEDS-SAR aims to optically reconstruct the SAR echo data on a laser beam and propagate it backward through free space, so that the echo energy converges to form a focused image in space. This process is, in essence, the physical inverse process of SAR data acquisition, replacing computational filtering with physical wave convergence.

From a signal processing perspective, this mechanism conceptually resembles the Back Projection (BP) algorithm in digital SAR processing. However, while the digital BP algorithm requires rasterizing the scene into discrete grids and computationally simulating the reverse transmission [11], the OEDS-SAR achieves this backward propagation physically in actual free space. Consequently, the scene does not need to be pre-rasterized, and the optical wavefront naturally converges to form the focused image.

The basic imaging principle is illustrated in the following Figure 5. As the radar platform flies along its flight path, it sequentially illuminates the target and receives echoes at different azimuth times, thereby forming a SAR receive array. Since the slant range $r(t)$ from the target to the radar varies with azimuth time, the echoes contain a phase history $-\frac{4\pi r(t)}{\lambda}$ that varies accordingly. This is the physical basis for SAR to achieve high-azimuth-resolution focusing.

As illustrated in Figure 6, the imaging mechanism of the OEDS-SAR can be further elaborated as follows: after range compression, the SAR data of point targets at different range gates manifest as azimuth signals distributed along migration curves in the X–Y

plane. These signals are loaded onto an SLM; when the SLM is illuminated by a laser beam, the echo information is encoded onto the wavefront of the reflected light [12,13]. As this beam propagates through free space, if there exists a point $P\ (X, 0, Z)$ in the focal plane such that the optical path differences from that point to each position along the migration curve exactly compensate for the original azimuth phase at each corresponding position, then that point is precisely the focused image corresponding to the migration curve [14].

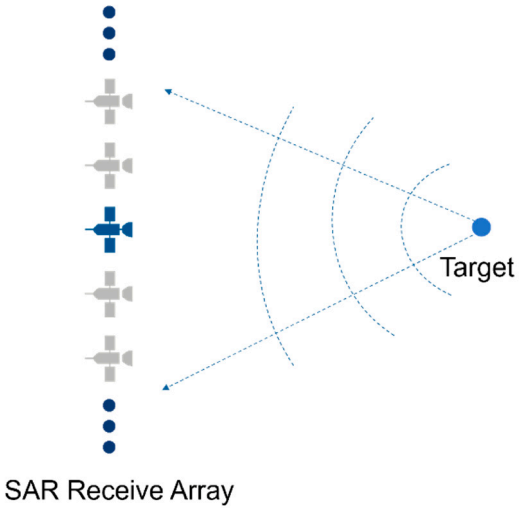


Figure 5. Schematic diagram of the basic imaging principle of OEDS-SAR.

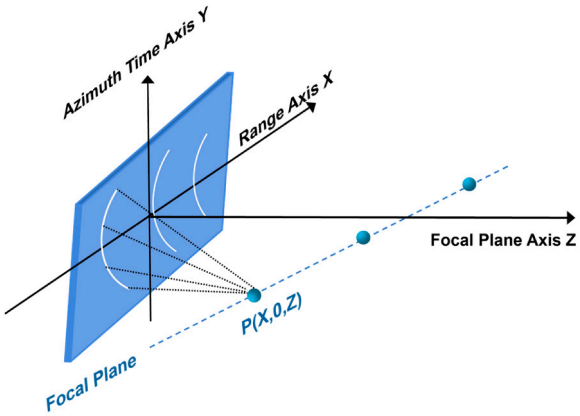


Figure 6. Schematic diagram of backward-propagation convergent imaging in the optical domain. X denotes the range axis (corresponding to the range direction of the SAR echo), Y denotes the azimuth time axis (corresponding to the slow-time direction of the SAR platform), and Z denotes the focal plane axis (representing the propagation direction of the light beam in free space).

In this way, the azimuth matched filtering—which would otherwise require complex algorithms in the digital domain—is transformed in the OEDS-SAR into the physical process of free-space propagation and phase compensation of light waves. The location of the image point can be determined either by direct calculation based on system parameters or by a search algorithm that identifies the focal plane with the optimal focusing quality.

3.2. SAR Echo Signal Model

We begin the derivation from the SAR echo signal after range compression. Consider a point-target scenario under broadside geometry; the SAR imaging geometry is shown in Figure 7.

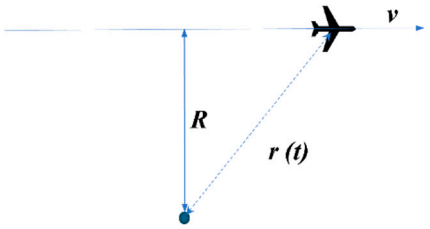


Figure 7. Simple linear flight geometry under the broadside assumption.

Under the assumption of a straight flight path and broadside geometry, the instantaneous slant range can be expressed as

$$r(t) = \sqrt{R^2 + v^2 t^2}, \tag{1}$$

and a typical point target SAR echo signal model [15,16] is given by

$$ss(\tau, t) = \mathrm{A}(\tau - \frac{2r(t)}{c}) \exp\left[-j\pi k\left(\tau - \frac{2r(t)}{c}\right)^2 + j2\pi f_c\left(\tau - \frac{2r(t)}{c}\right)\right] \tag{2}$$

where $k = B/T_p$ is the chirp rate (B: bandwidth, T_p: pulse width), A() is pulse envelope, τ is fast time, t is slow time, c is the speed of light, and f_c is the carrier frequency. It should be noted that Equation (2) describes the raw echo of a traditional pulsed radar system employing linear frequency-modulated (LFM) pulses. In the subsequent OEDS mapping, the data is already range-compressed, meaning the fast-time chirp term is removed, and only the azimuth phase history is retained for optical processing.

After down-conversion of the received SAR echo, the baseband signal is obtained as

$$ss_d(\tau, t) = \exp\left[-j\pi k\left(\tau - \frac{2r(t)}{c}\right)^2 + j2\pi f_c\left(\tau - \frac{2r(t)}{c}\right) - j2\pi f_c \tau\right] \tag{3}$$

$$ss_d(\tau, t) = \exp\left[-j\pi k\left(\tau - \frac{2r(t)}{c}\right)^2 - \frac{j4\pi r(t)}{\lambda}\right] \tag{4}$$

where $\lambda = c/f_c$ is the radar wavelength. Equation (4) clearly reveals the structure of the SAR baseband signal: the first term is the range chirp, which contains the target range information; the second term is the azimuth phase history term, $-\frac{4\pi r(t)}{\lambda}$, which contains all the azimuth phase information of the target. This latter term is the fundamental basis for achieving high azimuth resolution in SAR.

After range compression, the trajectory of a point target in the range–azimuth plane is the migration curve, as shown in Figure 8.

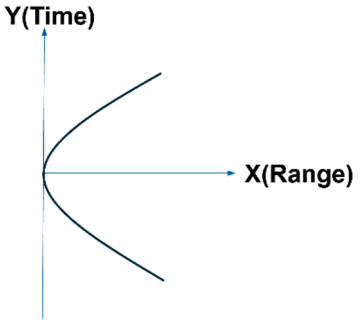


Figure 8. Typical migration curve.

At each azimuth time t along the migration curve, there exists a phase term

$$-\frac{4\pi r(t)}{\lambda} \tag{5}$$

The corresponding signal delay associated with this phase is

$$\frac{2r(t)}{c} \tag{6}$$

For data storage and processing, the minimum value is set to zero by removing the constant term corresponding to the closest range R, giving

$$\frac{2[r(t)-R]}{c} \tag{7}$$

Let the range sampling rate of the SAR system be f_s. The delay can then be converted into the number of sampling points

$$\frac{2[r(t)-R]}{c} f_s \tag{8}$$

3.3. SLM Pixel Mapping

To modulate the echo data onto the SLM, each range sampling point must be mapped to an SLM pixel. Let the SLM pixel pitch be Δ; the pixel position corresponding to the range delay is

$$r_p(t) = \frac{2[r(t)-R]}{c} f_s \Delta \tag{9}$$

Similarly, the azimuth direction is treated in the same manner. Each transmitted pulse at each pulse repetition interval (PRI) is mapped to one column of pixels on the SLM; the pixel position corresponding to azimuth time t is

$$\frac{t\Delta}{PRI} \tag{10}$$

Because SAR echo data are azimuth-symmetric under broadside geometry, we consider a point $P\ (X, 0, Z)$ in the optical X–Z plane of the (X, Y, Z) coordinate system, as depicted in Figure 6, such that the phase variation induced by the distances from P to each point on the migration curve is opposite to the original azimuth phase at each point, thereby achieving phase compensation. The SAR physical geometry coordinate system is composed of the range direction axis and azimuth time axis; in this system, the range direction and azimuth time are mapped to the X and Y axes, respectively, while the target position corresponds to the focal point P in the optical domain via the dual-reconstruction relationship.

The distance from P to the point on the migration curve at time t is

$$\sqrt{\left[X - r_p(t)\right]^2 + \left(\frac{t\Delta}{PRI}\right)^2 + Z^2} \tag{11}$$

if a plane wave of wavelength λ_0 is incident on the SLM, the phase difference accumulated when the reflected light propagates to point P is

$$\frac{2\pi}{\lambda_0}\sqrt{\left[X - r_p(t)\right]^2 + \left(\frac{t\Delta}{PRI}\right)^2 + Z^2} \tag{12}$$

substituting Equation (9) and introducing constant coefficients

$$k_1 = \frac{2f_s\Delta}{c},\ k_2 = \frac{\Delta}{PRI} \tag{13}$$

f_s is the sampling frequency in fast time. We obtain

$$\frac{2\pi}{\lambda_0}\sqrt{\left[X - k_1 r(t) + k_1 R\right]^2 + (k_2 t)^2 + Z^2} \tag{14}$$

Let $\boldsymbol{X} = X + k_1 R$. Then:

$$\frac{2\pi}{\lambda_0}\sqrt{[\boldsymbol{X} - k_1 r(t)]^2 + (k_2 t)^2 + Z^2} \tag{15}$$

Equation (15) indicates that for appropriate values of $\boldsymbol{X}$ and Z, this phase-difference expression can cancel the original azimuth phase $-\frac{4\pi r(t)}{\lambda}$ at each azimuth time along the migration curve. To physically illustrate this, as shown in Figure 9, the light beam reflected from different positions on the migration curve (corresponding to different azimuth times t) propagates towards a specific point $P(\boldsymbol{X}, 0, Z)$ in space. The varying optical path lengths from the SLM to point P introduce a spatial phase variation that is exactly opposite to the azimuth phase history. When the phase is completely compensated, the light waves from all azimuth times arrive in-phase at point P, constructing a coherent focal spot. This mathematically demonstrates that SAR echo signals can be focused into images through the OEDS-SAR system.

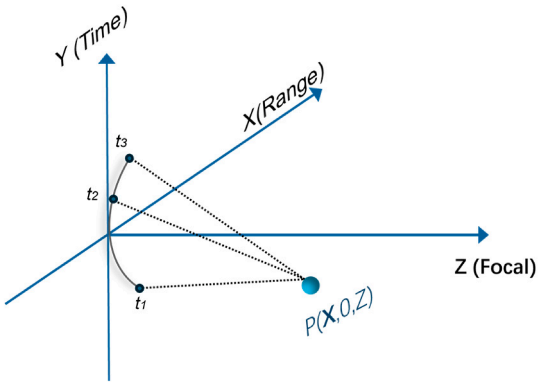


Figure 9. Schematic illustration of the phase compensation and focusing mechanism.

3.4. Dual Reconstruction

The previous subsection established the pixel mapping between the SAR echo and the SLM, and pointed out that if a point P $(X, 0, Z)$ can be found such that the phase difference introduced by the propagation distances from P to each point on the migration curve exactly cancels the original azimuth phase $-\frac{4\pi r(t)}{\lambda}$, then that point is the focused image point. Following this line of thought, we now determine the specific location of P through mathematical derivation.

Under the linear flight assumption, the instantaneous slant range can be expanded using a Taylor series and approximated as

$$r(t) = \sqrt{R^2 + v^2 t^2} \approx R + \frac{v^2 t^2}{2R} \tag{16}$$

The residual range error for the Taylor expansion is approximately $\Delta R \approx v^4 t^4/(8R^3)$. Over the synthetic aperture time $t \in [-T_{sa}/2, T_{sa}/2]$ (where T_{sa} is the total integration time of the target within the radar beam), the residual phase error is $\Delta\phi_r = \frac{4\pi}{\lambda}\Delta R$, and its maximum occurs at the edge of the aperture ($t = \pm T_{sa}/2$).

Consequently, the azimuth phase can be approximated as

$$-\frac{4\pi r(t)}{\lambda} \approx -\frac{4\pi R}{\lambda} - \frac{2\pi v^2 t^2}{\lambda R} \tag{17}$$

The first term in Equation (17) is a constant that does not affect focusing; therefore, only the second term (the t^2-dependent term) needs to be cancelled.

Expanding the square-root term in the distance expression from P to points on the migration curve

$$[k_1 r(t)]^2 + \boldsymbol{X}^2 - 2\boldsymbol{X}k_1 r(t) + (k_2 t)^2 + Z^2 \tag{18}$$

Substituting Equation (16) and separating into constant and t^2-dependent parts yields

$$k_1^2\left(R^2 + v^2t^2\right) + \boldsymbol{X}^2 - 2\boldsymbol{X}k_1\left(R + \frac{v^2t^2}{2R}\right) + k_2^2t^2 + Z^2 \tag{19}$$

Introducing the substitutions:

$$A^2 = \left(k_1^2R^2 + \boldsymbol{X}^2 - 2\boldsymbol{X}k_1R + Z^2\right) \tag{20}$$

$$B^2 = \left(k_1^2v^2 - 2\boldsymbol{X}k_1\frac{v^2}{2R} + k_2^2\right) \tag{21}$$

The azimuth phase history Equation (15) can then be written as

$$\frac{2\pi}{\lambda_0}\sqrt{A^2 + B^2t^2} = \frac{2\pi}{\lambda_0}\left(A + \frac{B^2t^2}{2A}\right) \tag{22}$$

The residual phase from the Fresnel expansion in Equation (22) is $\Delta\phi_a \approx \frac{2\pi}{\lambda_0}\frac{B^4t^4}{8A^3}$. Both Equations (16) and (22) rely on second-order Taylor/Fresnel approximations. In SAR processing, higher-order terms (e.g., cubic or quartic terms) are typically required only for highly squinted geometries to compensate for severe range–azimuth coupling [17–19]. Since our work is based on a broadside geometry, the second-order approximation is generally sufficient. Nevertheless, to rigorously validate this assumption, we quantify the maximum residual phase errors for both domains. Based on the parameters detailed in Section 4.4, the calculated maximum residual phase errors are summarized in Table 1.

Table 1. Quantitative analysis of maximum residual phase errors ($t = T_{sa}/2$).

Case	Integration Time T_{sa}	Residual Phase		Threshold $\pi/4$
		$\Delta\phi_{r_max}$	$\Delta\phi_{a_max}$	
Airborne	5.2 s	0.231 rad	0.195 rad	0.785 rad
Spaceborne	0.25 s *	0.00013 rad	0.563 rad	0.785 rad

* In spaceborne high-resolution modes, a sub-aperture processing strategy with 0.25 s is adopted to strictly preserve the paraxial approximation under high dynamic conditions.

As the results show, although there is a slight difference between the microwave and optical residual errors due to the truncation and scaled mapping, both results are well below the widely accepted threshold of $\pi/4$. Therefore, the paraxial approximation remains valid, and the higher-order terms will not cause significant defocusing.

Next, we evaluate the focusing condition. To achieve azimuth focusing, the following condition must hold:

$$\frac{2\pi}{\lambda_0} \times \frac{B^2t^2}{2A} = \frac{2\pi v^2t^2}{\lambda R} \tag{23}$$

This yields the focusing condition:

$$\frac{B^2}{A} = \frac{\lambda_0}{\lambda} \times \frac{2v^2}{R} \tag{24}$$

Substituting the expressions for A, B, $\boldsymbol{X}$, and after simplification, we obtain:

$$k_2^2 - 2Xk_1\frac{v^2}{2R} = \frac{2v^2\lambda_0}{\lambda R}\sqrt{X^2 + Z^2} \tag{25}$$

Let $x = v^2X$, $z = v^2Z$. Then obtain:

$$k_2^2 - \frac{xk_1}{R} = \frac{2\lambda_0}{\lambda R}\sqrt{x^2 + z^2} \tag{26}$$

Dividing both sides by v^2, and substituting the expressions for k_1, k_2, the focusing condition becomes:

$$\left(\frac{\Delta}{v \times PRI}\right)^2 = \frac{2\lambda_0}{\lambda}\frac{\sqrt{X^2 + Z^2}}{R} + \frac{X}{R}\frac{\Delta}{(c \times T_s)/2} \tag{27}$$

where $T_s = 1/f_s$ is the sampling interval. Equation (27) reveals several important scaling relations: $\Delta/(v \cdot PRI)$ represents the ratio between the unit distance in the azimuth direction on the SLM and the azimuth sampling interval of the actual SAR platform; $\Delta/((cT_s)/2)$ represents the ratio between the unit distance in the range direction on the SLM and the SAR range sampling distance; $2\lambda_0/\lambda$ represents the ratio between the optical wavelength and the microwave wavelength. The factor of 2 in these expressions accounts for the round-trip propagation characteristic of radar.

Equation (27) establishes a constraint between the system parameters and the focus coordinates. In real SAR imaging scenarios, however, different targets have different closest ranges R—nearby targets and distant targets may have R values differing by kilometers or even hundreds of kilometers. Therefore, we must understand how the focus position varies with R so that images of targets at different ranges can be correctly located in the optical system.

To investigate the variation of the focus point $P\ (X, 0, Z)$ with R, we introduce the following variable substitutions:

$$c^2 = \left(\frac{\Delta}{v \times PRI}\right)^2, a = \frac{2\lambda_0}{\lambda}, b = \frac{\Delta}{(c \times T_s)/2} \tag{28}$$

Equation (27) then simplifies to

$$c^2 = a\frac{\sqrt{X^2 + Z^2}}{R} + b\frac{X}{R} \tag{29}$$

By squaring both sides and rearranging

$$(a^2 - b^2)X^2 + a^2Z^2 + 2bc^2RX = \left(c^2R\right)^2 \tag{30}$$

dividing both sides by $(a^2 - b^2)$, and adding $\left(\frac{bc^2R}{a^2-b^2}\right)^2$ to both sides to complete the square

$$X^2 + \frac{a^2Z^2}{(a^2 - b^2)} + \frac{2bc^2RX}{(a^2 - b^2)} + \left(\frac{bc^2R}{a^2 - b^2}\right)^2 = \frac{\left(c^2R\right)^2}{(a^2 - b^2)} + \left(\frac{bc^2R}{a^2 - b^2}\right)^2 \tag{31}$$

we obtain the elliptic equation for the focus locus:

$$\left(X + \frac{bc^2R}{a^2 - b^2}\right)^2 + \frac{a^2Z^2}{(a^2 - b^2)} = \frac{\left(ac^2R\right)^2}{(a^2 - b^2)^2} \tag{32}$$

Equation (32) shows that the trajectory of the focus P is a quadratic curve in X and Z, and variations in R shift the center of the ellipse along the X-axis. We now examine the focus distribution in three cases.

Case 1: Z fixed—define $A = \frac{a^2}{a^2-b^2}$, $B^2 = \frac{(ac^2)^2}{(a^2-b^2)^2}$, $C = \frac{bc^2}{a^2-b^2}$, then Equation (32) reduces to

$$(X + CR)^2 + AZ^2 = (BR)^2 \tag{33}$$

$$X = \sqrt{(BR)^2 - AZ^2} - CR \tag{34}$$

This indicates that when Z is fixed, X is not linearly proportional to R, but follows a quadratic curve. The foci of point targets are non-uniformly distributed along the X-axis.

Case 2: X fixed—the relationship between Z and R becomes

$$AZ^2 = (BR)^2 - (X + CR)^2 \tag{35}$$

Z and R exhibit a nonlinear relationship. Cases 1 and 2 both show that the natural focus distribution is non-uniform, which is inconvenient for practical imaging—we need a more regular mapping.

Case 3: X varies linearly with R—let $X = -\frac{bc^2R}{a^2-b^2}$. Substituting this into Equation (32) gives

$$Z = \pm\frac{c^2R}{\sqrt{(a^2 - b^2)}} \tag{36}$$

Equation (36) shows that when X varies linearly with R, Z also becomes linearly related to R. Thus, a point target at range R will naturally focus at

$$\begin{cases} X = -\frac{bc^2R}{a^2-b^2} \\ Y = 0 \\ Z = \pm\frac{c^2R}{\sqrt{(a^2-b^2)}} \end{cases} \tag{37}$$

Equation (37) establishes a one-to-one linear correspondence between the radar-detected target coordinates $(R, 0, 0)$ and the optically reconstructed coordinates $(X, 0, Z)$. This correspondence is uniform and regular—targets farther away produce image points at proportionally farther positions. This is precisely the dual reconstruction from the microwave target space to the optical reconstruction space.

4. Implementation and Results

4.1. System Implementation

Based on the theoretical analysis above, the optical system is designed with an SLM to carry the SAR echo data, and a laser beam is used to read out the echo information and encode it onto the wavefront [20,21]: The SLM is an electro-optic conversion device, whose input is a digital signal. The digital data loaded onto the SLM is the range-compressed SAR echo, which is a complex matrix carrying the target's amplitude and azimuth phase information. And the liquid crystals on the SLM modulate the incident laser wavefront according to the amplitude and phase of the digital signal. Therefore, when the laser beam is incident on the SLM, the reflected laser beam carries the amplitude and phase information of the signal input to the SLM. This process can be regarded as the readout of the amplitude and phase information from the SLM by the laser beam.

Figure 10 shows the schematic diagram of the optical path, and Figure 11 presents both a three-dimensional schematic and a photograph of the actual optical system.

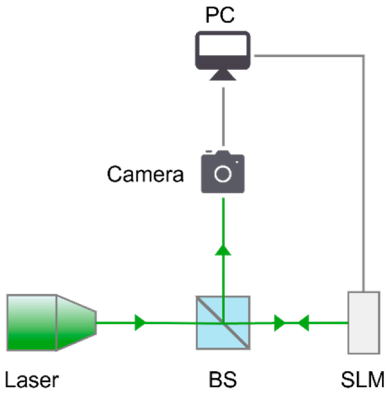
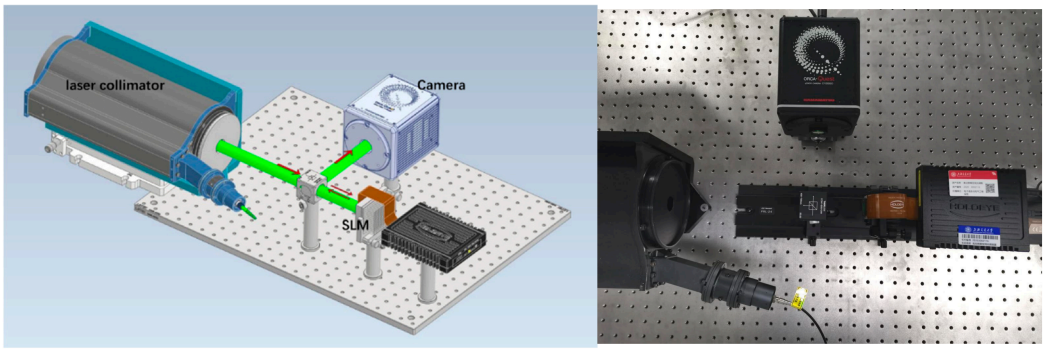


Figure 10. Schematic diagram of the optical path configuration.



(**a**) (**b**)

Figure 11. Optical system: (**a**) 3D model. (**b**) Physical photograph (Camera: ORCA-Quest C15550-22UP, Hamamatsu Photonics K.K., Hamamatsu, Japan).

4.2. Radar Waveform Parameters and Point-Target Validation

To validate the focusing capability of the OEDS-SAR system, a numerical simulation using MATLAB (v2021) was conducted using a typical pulse radar waveform (a transmitted bandwidth of 150 MHz, a pulse width of 10 μs, a carrier wavelength of 0.031 m).

Figure 12 presents the two-dimensional intensity distribution of a single point target after free-space propagation through the OEDS. As observed, the echo energy converges into a clear, diffraction-limited focal spot at the output plane, with the background remaining at a low intensity level. To further quantify the imaging quality and sidelobe suppression capability, the range and azimuth profiles of the point-target response are extracted and shown in Figure 13.

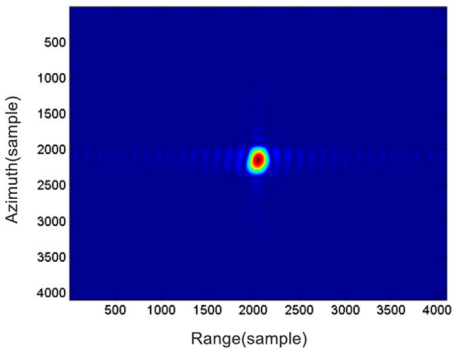
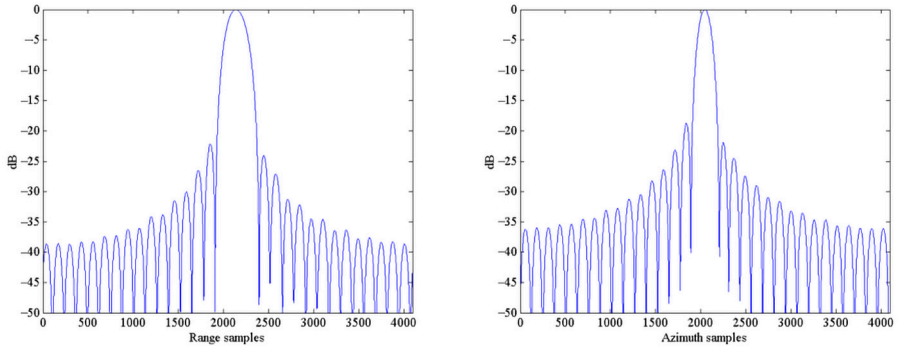


Figure 12. Two-dimensional intensity distribution of a single point target after free-space propagation.



(**a**) (**b**)

Figure 13. Point-target response profiles: (**a**) range profile; (**b**) azimuth profile.

Based on the profiles in Figure 13, the standard resolution metrics are evaluated. The Peak Side Lobe Ratio (PSLR) and Integrated Side Lobe Ratio (ISLR) are obtained as Table 2.

Table 2. Point-target standard resolution metrics.

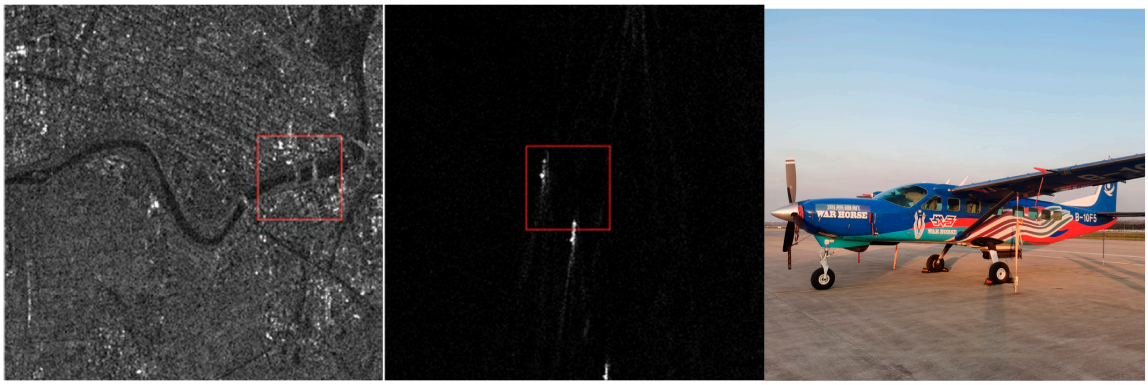
	Range Direction [1]	Azimuth Direction [2]
PSLR	−22.13 dB	−18.24 dB
ISLR	−20.02 dB	−15.61 dB

[1] Computed with digital pulse compression using a Kaiser window ($\beta = 2.71$). [2] Computed from the numerical simulation using second-order Taylor approximation.

These metrics indicate that the OEDS-SAR system achieves excellent sidelobe suppression and focusing performance, validating the theoretical derivations of the dual-reconstruction condition.

4.3. Real-Scene Imaging Results

To demonstrate the practical imaging capability of the OEDS-SAR system on realistic scenarios, our own real SAR data acquired in X-band with a resolution of 0.3 m were processed. Figure 14 presents the reconstructed optical-domain images.



(**a**) (**b**) (**c**)

Figure 14. Real-scene imaging results processed by the OEDS-SAR system and the data acquisition platform: (**a**) urban scene; (**b**) ship targets; (**c**) data acquisition platform (Cessna 208B Grand Caravan EX, Textron Aviation, Wichita, KS, USA, operated by Haiyan General Aviation).

As shown in Figure 14a, the urban scene exhibits clear structural details, including roads, buildings, and terrain features, demonstrating the system's ability to resolve complex

distributed targets. Figure 14b displays the imaging result of ship targets on the sea surface, where individual vessels can be distinctly identified against the low-backscatter background. These results confirm that the OEDS-SAR system, operating on actual SAR echo data rather than purely synthetic point-target models, can faithfully reconstruct real-world scenes in the optical domain. We summarize a quantitative comparison between the OEDS-SAR and conventional optical/digital processors in Table 3.

Table 3. Quantitative comparison between the OEDS-SAR and conventional optical/digital SAR processors.

Feature	Conventional Optical [9]	Digital Processors (RDA) [22]	OEDS-SAR (This Work)
Processing Mechanism	Mimics mathematical algorithms (matched filtering)	Executes numerical algorithms	Physical inverse reconstruction
Hardware Complexity	High (complex lens combinations)	High (large clusters of semiconductors)	Moderate (Laser, SLM, Camera)
Image Quality (Range PSLR)	−13 dB to −20 dB (depends on apodization)	−25 dB to −30 dB (depends on windowing)	−22.13 dB (with Kaiser window)
Programmability	Rigid	Highly flexible	Highly flexible
Processing Speed	>10 s (limited by mechanical film scanning)	~2.5 s (NVIDIA RTX 3060 GPU)	~10 ms (Pulse compression) <1 ns (Optical core) ~17 ms (Fixed System I/O)

The comparison is based on a large-scale SAR dataset (8192 × 8192). Conventional optics requires > 10 s due to mechanical film scanning. Digital RDA takes ~2.5 s on an RTX 3060 GPU and scales poorly with data size. In contrast, OEDS-SAR's digital pulse compression time is ~10 ms on the GPU, and optical core operates in <1 ns. In our physical setup, the total latency is ~17 ms, dictated by the SLM refresh rate (60 Hz, ~17 ms) and camera readout (120 frames/s, ~8.3 ms). Although electronic code execution depends on IDEs and optimizations (making exact millisecond comparison impractical), the order-of-magnitude difference is clear: OEDS-SAR operates on the millisecond scale, while both conventional optics and digital processors operate on the second scale for large scenes. This fundamentally demonstrates the speed superiority of our approach.

4.4. Parameter Analysis

Next, we analyze the implementation of the dual-reconstruction relationship under both spaceborne and airborne conditions [23,24]. In this section, we adopt a set of typical parameters (200 MHz bandwidth, 5 μs pulse width) slightly different from those in Section 4.2 in Tables 4 and 5 to systematically analyze the geometric dual-reconstruction mapping. The focus of this section is on the spatial coordinate scaling governed by velocity, range, *PRI*, and SLM pixel pitch.

Table 4. Airborne Simulation Parameters.

Parameter	Value	Parameter	Value
Radar Wavelength λ	3.125 cm	Range sampling rate f_s	1 GHz
Bandwidth B	200 MHz	Pulse width T_p	5 μs
Optical Wavelength λ_0	532 nm	Speed of light c	3×10^8 m/s
Platform Velocity v	100 m/s	Closest range R	10 km
SLM Pixel Pitch Δ	3 μm	*PRI*	1 ms

1. Airborne case. The main parameters for the airborne case are listed in Table 4.

Substituting these parameters into Equation (28) gives

$$c^2 = \left(\frac{\Delta}{v \cdot PRI}\right)^2 = \left(\frac{3 \times 10^{-6}}{100 \times 10^{-3}}\right)^2 = 9 \times 10^{-10}$$

$$a = \frac{2\lambda_0}{\lambda} = \frac{2 \times 532 \times 10^{-9}}{3.125 \times 10^{-2}} = 3.4 \times 10^{-5}$$

$$b = \frac{\Delta}{(cT_s)/2} = \frac{3 \times 10^{-6}}{3 \times 10^8 \times 10^{-9}/2} = 2 \times 10^{-5}$$

The focus positions are obtained as

$$\begin{cases} X = -2.38 \times 10^{-5} R \\ Y = 0 \\ Z = \pm 3.27 \times 10^{-5} R \end{cases}$$

In the airborne case, $R \sim 10^4$ m, so the coordinates $(X, 0, Z)$ are on the order of 0.1 m to 1 m.

2. Spaceborne case. The main parameters for the spaceborne case are listed in Table 5.

Substituting these parameters yields

$$c^2 = \left(\frac{\Delta}{v \cdot PRI}\right)^2 = \left(\frac{3 \times 10^{-6}}{7000 \times 10^{-3}}\right)^2 = 1.84 \times 10^{-13}$$

$$a = \frac{2\lambda_0}{\lambda} = \frac{2 \times 532 \times 10^{-9}}{3.125 \times 10^{-2}} = 3.4 \times 10^{-5}$$

$$b = \frac{\Delta}{(c \times T_s)/2} = \frac{3 \times 10^{-6}}{3 \times 10^8 \times 10^{-9}/2} = 2 \times 10^{-5}$$

The focus positions are

$$\begin{cases} X = -4.84 \times 10^{-9} R \\ Y = 0 \\ Z = \pm 6.67 \times 10^{-9} R \end{cases}$$

In the spaceborne case, $R \sim 6 \times 10^5$ m, so the coordinates are on the order of 1 mm to 10 mm.

To verify the paraxial condition in the spaceborne case, a short numerical check is performed using the Fresnel number (N_F):

$$N_F = \frac{(D/2)^2}{z\lambda_0} \tag{38}$$

where D is the SLM aperture size and z is the focal position ($z \approx 4$ mm). Assuming a typical SLM aperture of $D = 10$ mm, N_F is calculated as 11,748. Since $N_F \gg 1$, the optical system is well within the Fresnel diffraction regime, confirming that the short millimeter focal lengths do not violate the paraxial assumption.

3. Spaceborne case with reduced *PRI*. If the *PRI* is reduced to 0.1 ms (i.e., *PRF* increased to 10 kHz), then

$$c^2 = \left(\frac{\Delta}{v \cdot PRI}\right)^2 = \left(\frac{3 \times 10^{-6}}{7000 \times 10^{-4}}\right)^2 = 1.85 \times 10^{-11}$$

$$\begin{cases} X = -4.84 \times 10^{-7} R \\ Y = 0 \\ Z = \pm 6.67 \times 10^{-7} R \end{cases}$$

The coordinates are now on the order of 1 cm to 10 cm.

Table 5. Spaceborne Simulation Parameters.

Parameter	Value	Parameter	Value
Radar Wavelength λ	3.125 cm	Range sampling rate f_s	1 GHz
Bandwidth B	200 MHz	Pulse width T_p	5 μs
Optical Wavelength λ_0	532 nm	Speed of light c	3×10^8 m/s
Platform Velocity v	7 km/s	Closest range R	600 km
SLM Pixel Pitch Δ	3 μm	*PRI*	1 ms

The comparison of these three cases demonstrates that by appropriately selecting system parameters—particularly the *PRI* and the SLM pixel pitch—the OEDS-SAR system can achieve effective dual reconstruction under different platform conditions. The reconstructed coordinate scales vary systematically with the parameters, consistent with the theoretical analysis.

5. Conclusions

This paper proposed the Opto-Electronic Duality Principle (OEDP) and implemented the Opto-Electronic Duality System for SAR imaging (OEDS-SAR). The main conclusions are summarized as follows:

1. We constructed a physically equivalent inverse system of the microwave detection process. By mapping range-compressed SAR echo data onto an SLM, the system achieves azimuth focusing through physical wave convergence in free space, eliminating the need for complex digital matched filtering.
2. We derived the dual-reconstruction relationship between the SAR physical geometry and the optical domain. The quantitative analysis demonstrated that the Taylor/Fresnel approximations remain highly accurate, with maximum residual phase errors strictly controlled below the $\pi/4$ threshold for both airborne and spaceborne cases.
3. The system demonstrated excellent imaging performance. For the point-target simulation, the Range PSLR reached −22.13 dB and the Azimuth PSLR reached −18.24 dB. Moreover, real X-band SAR data processing confirmed the practical feasibility of the OEDS-SAR in reconstructing complex scenes.
4. Parameter analyses under different platform conditions verified the system's flexibility. By adjusting the digital inputs on the SLM, the identical optical hardware can be adapted to both airborne and spaceborne geometries, offering significant advantages in computational efficiency, low power consumption, and system simplicity compared to traditional digital and analog optical processors.

Future work will focus on extending the OEDS-SAR system to squint-mode geometries and larger-scale real-time processing applications.

6. Discussion

Previous foundational works on optical SAR processing established a paradigm that physically implements the mathematical algorithms (e.g., matched filtering or cross-correlation) of digital SAR processing using complex lens combinations (such as tilted-plane or 4f architectures). While highly effective, these systems essentially function as analog optical computers; their optical configurations are rigidly designed for specific radar parameters, making them difficult to adapt to varying operational conditions.

In contrast, this paper proposes a fundamentally different approach based on the OEDP. Instead of mimicking signal processing algorithms, the OEDS-SAR system is constructed as

a physically equivalent inverse system of the microwave detection process. By leveraging the inherent reversibility of light, the echo data are encoded onto a laser beam and propagated backward through free space, achieving azimuth focusing through physical wave convergence rather than computational filtering. Conceptually, this process is highly analogous to the BP algorithm in digital SAR, but it bypasses the need for digital scene rasterization. This design not only provides a strict dual-reconstruction relationship between the microwave and optical domains but also allows the identical optical hardware to be flexibly adapted to different airborne and spaceborne scenarios simply by updating digital inputs, as validated by our real X-band SAR data processing.

It should be noted that while the core optical propagation occurs at the speed of light, the overall throughput of the OEDS-SAR system is practically constrained by the electro-optic hardware interfaces, particularly the SLM refresh rate and camera readout latency (typically on the order of milliseconds). Nevertheless, compared to digital processors that require massive floating-point operations and high power consumption, the OEDS-SAR offers a significantly simplified hardware architecture.

Regarding spaceborne applications, the effective velocity v_{eq} should be substituted for the nominal platform velocity to account for Earth's rotation and orbit curvature. This substitution can be directly integrated into the derived equations without altering the core mapping framework. Furthermore, the millimeter-scale optical focal lengths are a direct consequence of the scale-down principle. Since the physical geometry is linearly mapped to the optical domain, the relative Fresnel number and paraxial conditions are preserved, ensuring the validity of the optical approximations even at short focal lengths. It should be noted that our current model assumes a broadside geometry; for squint-mode SAR, additional range walk compensation (linear phase terms) would be required, which will be addressed in future work.

Author Contributions: Conceptualization, H.Z. and K.W.; methodology, H.Z. and J.C.; resources, P.W.; data curation, J.D.; writing—original draft preparation, H.Z.; writing—review and editing, G.G.; project administration, Y.J. All authors have read and agreed to the published version of the manuscript.

Funding: This research received no external funding.

Institutional Review Board Statement: Not applicable. This study did not involve humans or animals.

Informed Consent Statement: Not applicable. This study did not involve humans.

Data Availability Statement: The data presented in this study are available on request from the corresponding author.

Conflicts of Interest: The authors declare no conflicts of interest.

References

1. Cruz, H.; Véstias, M.; Monteiro, J.; Neto, H.; Duarte, R.P. A review of synthetic-aperture radar image formation algorithms and implementations: A computational perspective. *Remote Sens.* **2022**, *14*, 1258. [CrossRef]
2. Denham, M.; Areta, J.; Tinetti, F.G. Synthetic aperture radar signal processing in parallel using GPGPU. *J. Supercomput.* **2016**, *72*, 451–467. [CrossRef]
3. Cutrona, L.J.; Leith, E.N.; Porcello, L.J.; Vivian, W. On the application of coherent optical processing techniques to Synthetic-Aperture radar. *Proc. IEEE* **1966**, *54*, 1026–1032. [CrossRef]
4. Leith, E.N. Optical processing techniques for simultaneous pulse compression and beam sharpening. *IEEE Trans. Aerosp. Electron. Syst.* **1968**, *AES-4*, 879–885. [CrossRef]
5. Wang, D.; Zhang, Y.; Yang, C.; Wang, K. Study on processing synthetic aperture radar data based on an optical 4f system for fast imaging. *Opt. Express* **2022**, *30*, 44408–44419. [CrossRef]
6. Zhao, H.; Zhang, X.; Wang, D.; Bi, G.; Fu, T. Optical-mechanical system design of SAR real-time imaging optical processor. *Opto-Electron. Eng.* **2022**, *49*, 210421.

7. Cai, Z.; Zhang, X.; Chen, Z.; Bi, G.-L.; Wang, H.-J. New SAR real-time imaging optical system design. *Chin. J. Liq. Cryst. Disp.* **2020**, *35*, 1185–1194. [CrossRef]
8. Wang, D.; Ou Yang, R.; Wang, K.; Fu, T.; Jin, L.; Bi, G.; Zhang, X. Optical SAR data processing configuration with simultaneous azimuth and range matching filtering. *Appl. Opt.* **2020**, *59*, 10441–10450. [CrossRef]
9. Kozma, A.; Leith, E.N.; Massey, N.G. Tilted-Plane optical processor. *Appl. Opt.* **1972**, *11*, 1766–1777. [CrossRef]
10. Leith, E.N. Quasi-Holographic techniques in the microwave region. *Proc. IEEE* **1971**, *59*, 1305–1318. [CrossRef]
11. Munson, D.C.; O'Brien, J.D.; Jenkins, W.K. A tomographic formulation of Spotlight-Mode synthetic aperture radar. *Proc. IEEE* **1983**, *71*, 917–925. [CrossRef]
12. Johnson, K.M.; McKnight, D.J.; Underwood, I. Smart spatial light modulators using liquid crystals on silicon. *IEEE J. Quantum Electron.* **1993**, *29*, 699–714. [CrossRef]
13. Yang, Y.; Forbes, A.; Cao, L. A review of liquid crystal spatial light modulators: Devices and applications. *Opto-Electron. Sci.* **2023**, *2*, 230026. [CrossRef]
14. Yang, C.; Zhang, Y.; Wang, D.; Wang, K. Compact optical real-time imaging system for high resolution SAR data based on autofocusing. *Opt. Commun.* **2023**, *546*, 129751. [CrossRef]
15. Eldhuset, K. A new Fourth-Order processing algorithm for spaceborne SAR. *IEEE Trans. Aerosp. Electron. Syst.* **1998**, *34*, 824–835. [CrossRef]
16. Raney, R.K.; Runge, H.; Bamler, R.; Cumming, I.; Wong, F. Precision SAR processing using chirp scaling. *IEEE Trans. Geosci. Remote Sens.* **1994**, *32*, 786–799. [CrossRef]
17. Moreira, A.; Huang, Y. Airborne SAR processing of highly squinted data using a chirp scaling approach with integrated motion compensation. *IEEE Trans. Geosci. Remote Sens.* **1994**, *32*, 1029–1040. [CrossRef]
18. Wong, F.H.; Yeo, T.S.; Tan, N.L. New applications of Non-Linear chirp scaling in SAR data processing. In Proceedings of the IGARSS 2000. IEEE 2000 International Geoscience and Remote Sensing Symposium, Honolulu, HI, USA, 24–28 July 2000.
19. Wang, K.; Liu, X. Quartic-Phase Algorithm for Highly Squinted SAR Data Processing. *IEEE Geosci. Remote Sens. Lett.* **2007**, *4*, 246–250. [CrossRef]
20. Jin, Y.; Guo, R.; Gao, Y.; Wang, K.; Liu, X.; Lin, C.; Wang, H. A tiling of multi-SLM is used in full resolution optical SAR data processor. In *Proceedings of the 2014 IEEE Geoscience and Remote Sensing Symposium, Quebec City, QC, Canada, 13–18 July 2014*; IEEE: Piscataway, NJ, USA, 2014; pp. 588–591.
21. Zhang, J.; Gao, Y.; Wang, K.; Liu, X. An optical SAR data processor based on DMD. In *Proceedings of the 2016 Progress in Electromagnetic Research Symposium (PIERS), Shanghai, China, 8–11 August 2016*; IEEE: Piscataway, NJ, USA, 2016; pp. 2893–2897.
22. Cumming, I.G.; Wong, F.H. *Digital Processing of Synthetic Aperture Radar Data: Algorithms and Implementation*; Artech House: Boston, MA, USA, 2005; pp. 156–172.
23. Bourqui, P.; Harnisch, B.; Marchese, L.; Bergeron, A. Optical SAR processor for space applications. *Sens. Syst. Space Appl. II* **2008**, *6958*, 134–143. [CrossRef]
24. Zhao, P.; Wang, K.; Liu, X. A novel high resolution optical SAR processor for satellite applications. In Proceedings of the 2013 IEEE International Geoscience and Remote Sensing Symposium (IGARSS), Melbourne, VIC, Australia, 21–26 July 2013; IEEE: Piscataway, NJ, USA, 2013; pp. 2900–2903.

Disclaimer/Publisher's Note: The statements, opinions and data contained in all publications are solely those of the individual author(s) and contributor(s) and not of MDPI and/or the editor(s). MDPI and/or the editor(s) disclaim responsibility for any injury to people or property resulting from any ideas, methods, instructions or products referred to in the content.